Contents lists available at ScienceDirect

Applied Surface Science

Full Length Article

Reconfigurable localized surface plasmon resonance spectrum based on acousto-dynamic coupling in arrays gold nanoparticles induced by shear horizontal vibration

Teguh Firmansyah [a,b,*], Gunawan Wibisono [b], Eko Tjipto Rahardjo [b], Jun Kondoh [a,c,*]

[a] Graduate School of Science and Technology, Shizuoka University, 3-5-1 Johoku, Naka-Ku, Hamamatsu-shi, Shizuoka 432-8561, Japan
[b] Department of Electrical Engineering, Universitas Indonesia, Kampus Baru UI Depok, Depok, West Java 16424, Indonesia
[c] Graduate School of Integrated Science and Technology, Shizuoka University, 3-5-1 Johoku, Naka-Ku, Hamamatsu-shi, Shizuoka 432-8561, Japan

ABSTRACT

Reconfigurable localized surface plasmon resonance (LSPR) is an essential characteristic for various applications to support Society 5.0. However, many LSPR spectrum have poor reconfigurability. As a novelty, we proposed a reconfigurable LSPR spectrum by acousto-dynamic coupling in arrays of gold nanoparticles (AuNPs) induced by shear-horizontal vibrations. The vibrations were produced by piezoelectric phenomena especially shear horizontal surface acoustic waves (SH-SAWs) on a 36XY-LiTaO$_3$ substrate after applying an electric signal, the ON-condition. The experimental results demonstrated that the ON-condition produced a blueshift effect on the peak position (λ_P) with an adjustment quality factor compared to the OFF-condition. Moreover, in order to perform the finite-difference time-domain (FDTD) analysis, we reproduced the morphological structure of AuNPs base on scanning electron microscope (SEM) images. The different coupling distances and different arrays structures were utilized as ON-condition approaches for dimer AuNPs and arrays AuNPs, respectively. The FDTD simulation obtained a blueshift effect compared to the initial structure. Finally, the proposed structure successfully combines piezoelectric phenomena with plasmonic phenomena to produce reconfigurable LSPR. The LSPR spectrum can be switched comfortably and reverses easily. The proposed method can be applied for multifunctional sensors with the high possibility of integration into a wireless network.

1. Introduction

A localized surface plasmon resonance (LSPR) effect refers to the collective oscillation of the conduction electron band in a metallic nanoparticle (MeNP) structure while it interacts with a specific wavelength of incident light [1,2]. A reconfigurable LSPR spectrum is an essential parameter for biochemistry, energy, electronics, and sensor applications to support Society 5.0 and strengthen programs for sustainable development goals (SDGs). However, there are still many LSPR applications that lack configurability performance. The LSPR spectrum band is influenced by the particle size, aspect ratio, shape, material structure, surrounding dielectric, and interparticle distance [3–7]. Therefore, numerous studies have been conducted to modify the LSPR spectrum based on the particle size, aspect ratio, shape, material structure, and surrounding dielectric to maximize the functionality of the LSPR effect [8–15].

Various methods can be used to modify LSPR spectrum [16–18]. In detail, we can separate as two primary classifications strategy: during fabrication and post-fabrication methods, which can generate a static LPSR resonant and a dynamic LPSR resonant, respectively. Moreover, a post-fabrication method gives advantages such as a reconfigurable LPSR capability. A post-fabrication method is commonly developed based on deformable substrates such as polydimethylsiloxane (PDMS) by applying mechanically stretch. Therefore the metal nanoparticle structure or interparticle distances of gold-nanodisks [19] or silver-nanodisks [20] can be modified. Furthermore, the mechanism was successfully expanded by Mizuno et al [21] using uniaxial and biaxial strain to obtain high monotonous peak and wavelength shift.

Another interesting post-fabrication reconfigurable LSPR spectrum method is based on hydrogel membrane exchange [22,23]. The main idea of membrane injection is to change the refractive index of the surrounding environment using hydrogel aqueous materials. Therefore,

---

the fully switching OFF-ON of the LSPR resonances is obtained. Moreover, another post-fabrication attractive method is using liquid crystals (LCs) matrix [24,25]. The LCs matrix has an adjustable optical property by changing the molecular orientation using an external trigger such as an electric field. Therefore, the combination of LCs with gold-nanorods [24] or gold-nanodots [25] induced by an external electric field can produce a reconfigurable LSPR spectrum.

In their experiments, the reconfigurable LSPR spectrum based on the post-fabrication method was successfully obtained. However, the use of mechanical stretch by a mechanical actuator is inconvenient for practical applications because an additional external motor needs to control the strain precisely. Moreover, the changing environment using hydrogel aqueous materials or the inducing electric field into LCs matrix is also difficult because it involves wet material where a simple and dry condition is desired, especially for mass production.

As novelty, we propose reconfigurable LSPR spectrum based on acousto-dynamic coupling in arrays AuNPs induced by shear horizontal vibration as shown in Fig. 1(a). The shear horizontal vibrations are produced by a piezoelectric phenomenon. Although there are some studies about the interactions between plasmonic devices and piezoelectric materials [26–28]. However, there have been no reports of obtaining a reconfigurable LSPR spectrum using shear horizontal. In more detail, the contributions of this study are as follows:

1. A reconfigurable LSPR spectrum was designed by acousto-dynamic coupling in arrays gold nanoparticles induced by shear horizontal vibration. The vibrations were generated by shear-horizontal surface acoustic waves (SH-SAWs) on a 36XY-LiTaO$_3$ substrate after applying an electric signal via interdigital transducers (IDTs), as shown in Fig. 1(b). The existence of SH-SAWs stimulates dynamic changes in the structure of the arrays AuNPs. This leads to a reconfigurable LSPR spectrum.
2. A reconfigurable LSPR means that the wavelength position of the peak (λ_P) and the quality factor (Q-factor) of the LSPR spectrum can switch comfortably and can also be easily reversed to their original position. Comprehensive examinations were performed, such as atomic force microscopy (AFM), scanning electron microscopy (SEM) imaging, electrical characterization via a vector network analyzer, and reconfigurable and reversible LSPR spectrum analysis using a UV–vis spectrophotometer.
3. The experimental results demonstrated that the ON-condition produced a blueshift effect on λ_P with an adjusted Q-factor compared to

the OFF-condition. The measured LSPR spectrum can be switchable comfortably and reversed easily.
4. Moreover, in order to perform the finite-difference time-domain (FDTD) analysis, we reproduced the morphological structure of AuNPs on the 36XY-LiTaO$_3$ substrate based on SEM images, as shown in Fig. 1(c). In detail, the structures were separated into three classifications such as; identical dimer AuNPs, nonidentical dimer AuNPs, and arrays AuNPs structure. Then, the initial AuNPs structure was used as an OFF-condition. Furthermore, the different coupling distances and different arrays structures were utilized as ON-condition approaches for dimer AuNPs and arrays AuNPs, respectively. The FDTD simulation was used to examine the plasmonic enhanced near field and LSPR spectrum.
5. Finally, the proposed structure successfully combines piezoelectric phenomena with plasmonic phenomena to produce reconfigurable LSPR. The LSPR spectrum can be switched comfortably and reverses easily. Moreover, the proposed method can be applied for multifunctional sensors with the possibility of integration into a wireless network.

The remainder of this paper is organized as follows. The measurement results for the reconfigurable LSPR spectrum induced by shear horizontal vibration are elucidated in Section 2. Fabrication and the morphological characterization of AuNPs on the piezoelectric substrate including AFM and SEM imaging are presented in Section 3. Furthermore, FDTD computational LSPR analysis of identical dimer AuNPs, nonidentical dimer AuNPs, and arrays AuNPs on the 36XY-LiTaO$_3$ substrate is explained in Section 4. Finally, Section 5 provides the concluding remarks.

2. Measurement of reconfigurable LSPR spectrum induced by shear horizontal vibration

This section is explained the measurement results for the reconfigurable LSPR spectrum induced by shear horizontal vibration. Moreover, the first explanation will focus on the surface acoustic waves (SAWs) mechanism in vibrating arrays AuNPs. Then, it is followed by a complete measurement of a reconfigurable LSPR spectrum. Finally, the effect of the different driving signals, including DC voltage is explained at the last this section.
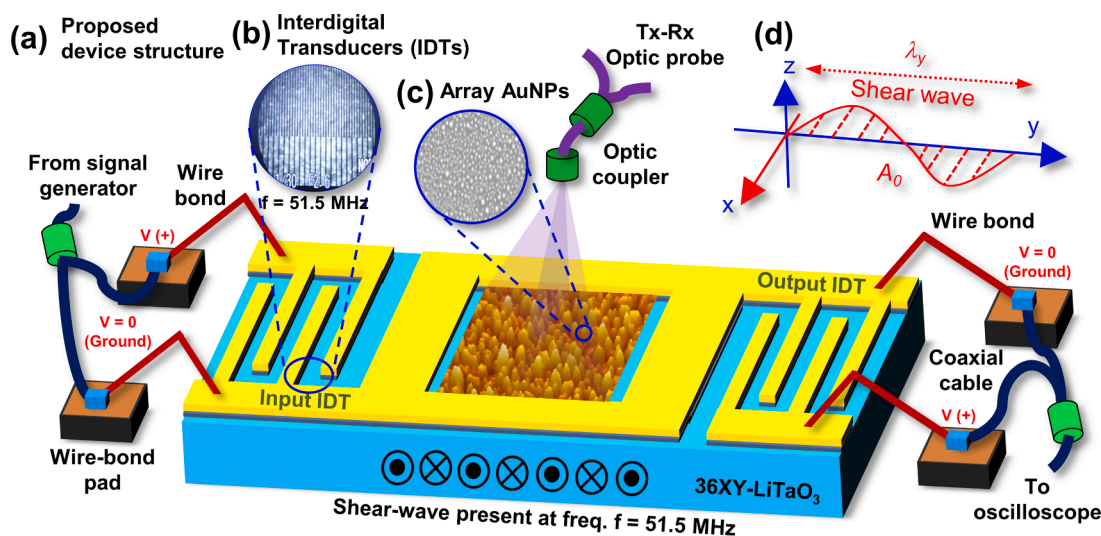

Fig. 1. (a) A proposed device structure of reconfigurable LSPR spectrum based on acousto-dynamic coupling array AuNPs induced by shear horizontal vibration, (b) Interdigital transducers were designed at frequency of 51.5 MHz, (c) 2D-SEM image of array AuNPs on the propagation surface of SH-SAW, (d) the shear-horizontal surface acoustic waves excited on a 36XY-LiTaO$_3$ substrate after applying an electric signal via interdigital transducers.

2.1. The SAWs mechanism in vibrating arrays AuNPs

The surface acoustic waves on a piezoelectric material can be separated into two major classifications: Rayleigh waves and shear horizontal waves. A Rayleigh wave has a Rayleigh mode and generates longitudinal waves, as depicted in Figs. S1(a-b). However, we propose to employ the shear horizontal vibrations formed by SH-SAWs on a 36XY-LiTaO$_3$ substrate to obtain acousto-dynamic coupling in arrays AuNP. In detail, SH-SAWs were generated from the IDT by applying an electric signal. Fig. 1(d) shows the coordinate system of particle displacement from the piezoelectric effect for the surface shear wave condition which is follow the wave equation [29]. It is given by $U_x(y,z,t) = A_0 e^{-\beta_s y} \cos(\omega t - k_{sr} y)$, where $U_x(y,z,t)$ denotes the displacements in the x- and z-directions, A_0 is the maximum amplitude of the $U_x(y,z,t)$ displacement in the x-direction, β_s is the damping coefficient in the y-direction, $\omega = 2\pi f$ rad/s, t denotes the time, and k_{sr} is the real wavenumber. These waves propagate along the y-direction with wavelength λ_y, which is determined by $\lambda_y = 2\pi/k_{sr}$. Several notes can be elucidated such as the value of A_0 depends on the applied input voltage, and the oscillation frequency depends on the frequency of the input voltage. Therefore, we can control the shear surface wave $U_x(y,z,t)$ by controlling the input voltage and working frequency with an appropriate IDT structure.

Here, we design the IDT structure to resonate at a frequency of 51.5 MHz. Then, to exciting the shear wave vibration, it should be supplied an electric signal (RF signal) with the same frequency of 51.5 MHz. As a result, the shear wave vibration will oscillate at a frequency of 51.5 MHz on a surface of 36XY-LiTaO$_3$. If there is a different condition between the IDT design structure and the input signal, the shear wave would not be generated.

Fig. 2(a) shows an electric input signal from a signal generator separated as OFF-condition and ON-condition (V_{P-P}). The OFF-condition has a value of $V_{P-P} = 0$ V, then the ON-condition has a sine wave shape with a value of $V_{P-P} = 2$ V and a frequency of 51.5 MHz. In other words,

it has RF input signal. Fig. 2(b) illustrates a side view of IDT with the electrical potential for OFF-condition. An OFF-condition is not excited the shear waves. Therefore, the arrays AuNPs have a static condition or not change, as shown in Fig. 2(c). In contrast, Fig. 2(d) shows the side view of IDT with the electrical potential for ON-condition. At ON-condition, the positive and negative potentials will appear alternately with the frequency of 51.5 MHz. Therefore, the shear-wave is excited. The appearance of the shear wave causes vibration of arrays AuNPs structure, as shown in Fig. 2(e).

2.2. Measurement of reconfigurable LSPR spectrum

A complete measurement of a reconfigurable LSPR spectrum is described in this section. First, to measure the LSPR spectrum, an un-polarized halogen light (Model: 5–2300, Soma Optics, Ltd. Japan) with a wavelength ranging from 350 to 1000 nm was used as the light source. It was connected using flexible fiber optics with a length of 2 m (P400-2-VIS-NIR, Ocean optics, Inc., USA). An optical probe holder (Chuo Seiki, Japan) was utilized. A USB4000 UV–vis spectrophotometer (Ocean Optics, Inc., USA) was used and connected to a computer. OPwave + software with recoded capability was installed on the computer. Text-to-Excel conversion and MS-Excel were used for converting, visualizing, and analyzing the data.

A reflectance measurement method was used because the 36XY-LiTaO$_3$ substrate is not transparent due to polished. This reflectance method was performed for the LSPR [30–34], and the reflectance was obtained using the equation of $R_r = I_s/I_r$, where R_r is the reflectance value (au.), I_s is the intensity of the sample, and I_r is the intensity of the reference. The normalized value was calculated to determine the peak position under clear conditions. Then, a WF1967 multifunction signal generator (NF Corporation., Japan) was used as the electrical input signal. A sine wave with a frequency of 51.5 MHz was selected with various voltages. This signal generator was connected to the device using a coaxial cable, AV-Part (T-sin, Japan), with a sample pad based on
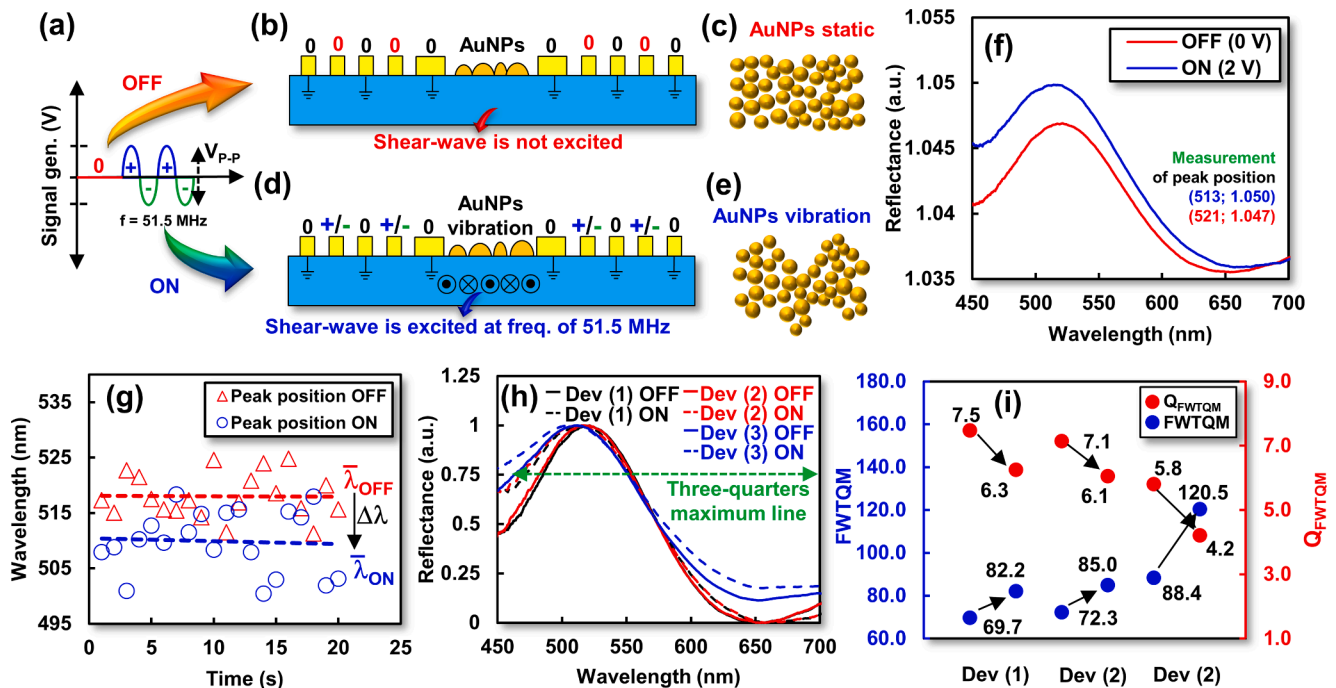

Fig. 2. (a) Electric input signal from signal generator with OFF-condition and ON-condition (V_{P-P}) with frequency of 51.5 MHz, (b) side view of IDT with the electrical potential for OFF-condition, the shear-wave is not exciting, (c) array AuNPs structure for OFF-condition, (d) side view of IDT with the electrical potential for ON-condition, the shear-wave is exciting at frequency of 51.5 MHz, (e) array AuNPs structure for ON-condition, (f) the reflectance of the LSPR spectrum at the OFF/ON-condition, (g) the measurement and data acquisition procedures for the reconfigurable LSPR spectrum, (h) the normalization of the LSPR spectrum reflectance at the OFF/ON-condition, and (i) an investigation of the effects of the OFF/ON conditions on the FWTQM and Q$_{FWTQM}$ factor.

a Sigma holder (Sigma, Japan). At the output port of the IDT, the device was connected to an InfiniVison MSKOX4033A oscilloscope (Keysight, USA).

The reflection was measured on the SH-SAWs with AuNPs only because the SH-SAWs without AuNPs did not produce the LSPR effect. The wavelength position of the peak has two positions under OFF or ON conditions. The SH-SAW was generated by the electric signal with the input voltage of $V_{P-P} = 2$ V at the frequency of 51.5 MHz. The OFF position corresponded to the opposite situation, as shown in Fig. 2(f). In detail, Fig. 2(g) shows the twenty measurements acquired over one minute (recorded every 3 s) and then averaged. To make the data more robust, we repeated this procedure on three devices, namely, Dev (1), Dev (2), and Dev (3), as shown in Fig. 2(h). The peak positions in the OFF condition were observed at 521, 516, and 513 nm, and those in the ON condition were observed at 513, 514, and 507 nm with Dev (1), Dev (2), and Dev (3), respectively. Based on these measurements, we observe the fascinating result that the peak position of the reflection was robustly and consistently blueshifted. We attributed this effect to the changes in the AuNP arrays structure. Here is the explanation. First, the SH-SAWs generated shear horizontal vibrations. Then, the vibrations changed the arrays AuNPs configuration. The change in the arrays AuNPs configuration resulted in a change in the plasmonic enhanced near field interaction. Then, it led to a blueshift peak effect.

In addition to an examination of the λ_P position, we also evaluated the quality factor for more comprehensive data. Fig. 2(h) shows the normalization of the LSPR spectrum reflectance at the OFF/ON-condition. Besides, we also propose a new term called the full-width at three-quarter maximum (FWTQM) to evaluate a quality factor of the LSPR spectrum. The FWTQM is defined by the wavelength position when it reaches 75% of the peak. Then, the quality factor using the FWTQM (Q_{FWTQM}) can be given by $Q_{FWTQM} = \lambda_P/FWTQ$, where Q_{FWTQM} is the Q-factor value at 75% of the peak, λ_P is the peak position, and FWTQM = $\lambda_{UB} - \lambda_{LB}$, with λ_{UB} being the 75% peak upper band and λ_{LB} being the 75% peak lower band. The results of investigating the quality factor under the OFF and ON conditions are illustrated in Fig. 2(i).

In detail, Fig. 2(i) shows that the FWTQM for OFF and ON conditions was 69.7 nm and 82.2 nm, 72.3 nm and 85.0 nm, and 88.4 nm and 120.5 nm, for Dev (1), Dev (2), and Dev (3), respectively. The Q_{FWTQM} factors

under the OFF and ON conditions were 7.5, 6.3, 7.1, 6.1, 5.8, and 4.2 for Dev (1), Dev (2), and Dev (3), respectively. The SH-SAW effect changed the AuNP inter distance and generated a blueshift along with a larger bandwidth and lower Q_{FWTQM} factor.

To obtain more comprehensive results, we also measured the LSPR response for different input electric signals of the peak-peak voltage (V_{P-P}), such as 4 V, 6 V, 8 V, and 10 V, with an RF signal frequency of 51.5 MHz. It is important to mention that the input voltage has a direct connection with the particle displacement amplitude of the SH-SAWs. Therefore, a precise synchronization measurement is required to observe the comparison of the LSPR spectrum between two different voltages. Precise synchronization means that the LSPR measurement should be performed by equalizing the captured times of reflection and oscillation of the shear wave or that it should have a frequency of 51.5 MHz. However, the devices used in our measurements were limited from retrieving this type of data. Therefore, we proposed an alternative robust method by comparing the results for different voltages to the zero-voltage condition as a reference. In other words, we have expanded the OFF (0 V)/ON (2 V) concept to a more general concept by using OFF (0 V) as the initial position. This strategy is named the reconfigurable LSPR method.

In detail, the reconfigurable LSPR spectrum based on different voltages signal of 0 V/2 V, 0 V/2 V/6 V, and 0 V/8 V/10 V, are shown in Fig. 3(a), 3(b), and 3(c), respectively. The results demonstrate that the comparison between the OFF and ON (2 V/4 V/6 V/8 V/10 V) conditions produced a higher reflection value with a shorter wavelength; that is, it had a blueshift effect. Using this method, we obtained robust data that showed that the change in the input voltage was affected by different-amplitude shear horizontal surface waves that could adjust the AuNP arrays structure and lead to reconfiguration of the LSPR spectrum. Moreover, Fig. 3(d) shows the peak wavelength position with different input voltages for Dev (1), Dev (2), and Dev (3). We can see that the blueshift was obtained consistently compared to references or peak wavelength at OFF-condition (V = 0). Finally, we confidently concluded that a reconfigurable LSPR spectrum was successfully developed. More specifically, the proposed method can comfortably switch the λ_P and Q_{FWTQM} of the LSPR spectrum, and it can also be easily reversed to its original position.
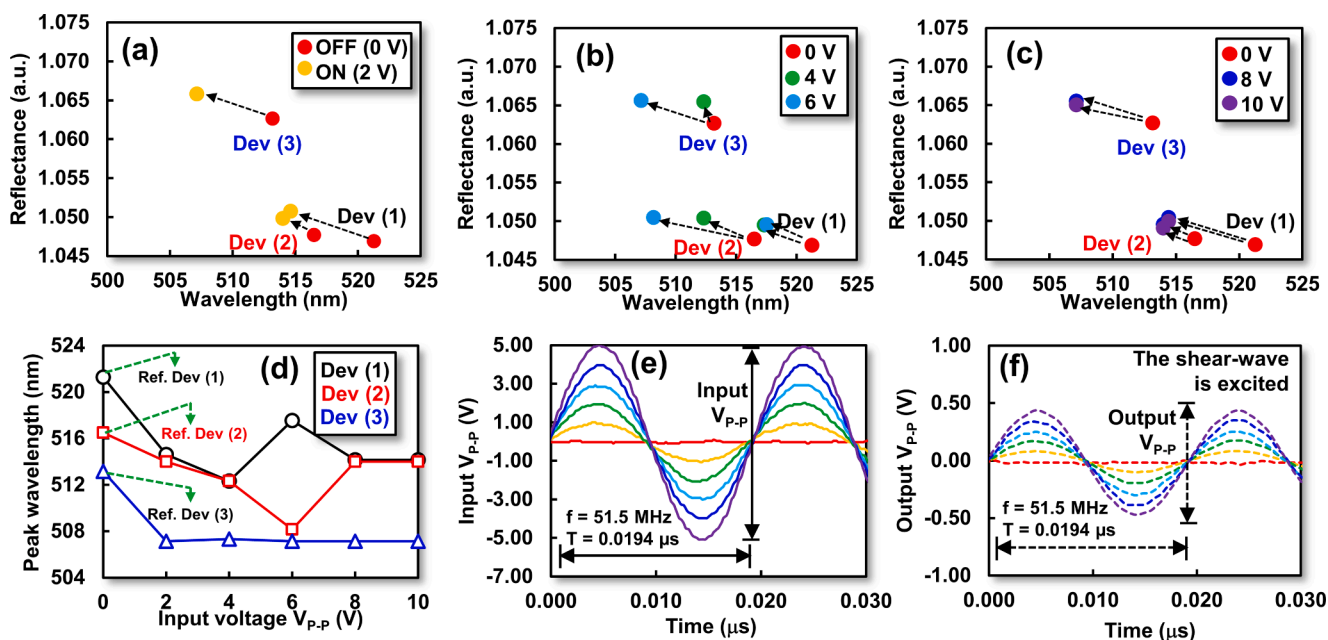

Fig. 3. The reconfigurable LSPR spectrum based on the OFF/ON sine signal at (a) 0 V/2 V, (b) 0 V/2 V/6 V, and (c) 0 V/8 V/10 V. (d) the peak wavelength position with different input voltages for Dev (1), Dev (2), and Dev (3), (e) the RF input signal at frequency of 51.5 MHz with voltage variation of V_{P-P} from 2 V, 4 V, 6 V, 8 V, and 10 V, (f) the RF output signal at input frequency of 51.5 MHz.

2.3. The effect of different driving electric input signal

As mentioned above, we designed the IDT structure to resonate at a frequency of 51.5 MHz. Therefore, an RF signal should be supplied with a frequency of 51.5 MHz to excite the shear wave vibration. Fig. 3(e) shows the RF input signal at 51.5 MHz with voltage variation V_{P-P} from 2 V, 4 V, 6 V, 8 V, and 10 V. Then, Fig. 3(f) illustrates the RF output signal. We can see that the output voltage has a high value with the same frequency as the input. Therefore, the measurement result was indicated that the piezoelectric phenomena occurred. Then, we can conclude that the shear-wave vibration excites successfully.

Moreover, Fig. S2(a) shows the RF input signal at 36.5 MHz with voltage variation V_{P-P} from 2 V to 10 V. It should be noted that the RF input signal has a lower frequency than the IDTs operation. Then, the RF output signal is shown in Fig. S2(b). In the opposite position, Fig. S2(c) shows the RF input signal at 66.5 MHz, or it has a higher frequency than the IDTs operation. The output RF signal is shown in Fig. S2(d). We can see that both RF input signals have high voltage values, as shown in Figs. S2(a) and S2(c). However, the result indicates that both RF output signals have small voltage, as shown in Figs. S2(b) and S2(d). This result is indicated that the share-waves vibration is not excited. This condition happened because the RF input signal frequency did not match with the IDT design structure. Besides, the function of IDTs as a resonator becomes ineffective. This circumstance will lead the piezoelectric crystal to the nonlinear condition. The nonlinear condition of piezoelectric occurs when electric field, strain, and dielectric responses become nonlinear [35,36]. Therefore, it is important to note that our research was focused on the linear condition of piezoelectric to make sure that the arrays AuNPs have vibration smoothly.

Fig. S2(e) shows the DC input signal with V_{P-P} voltage from 2 V, 4 V, 6 V, 8 V, and 10 V. Then, the DC output signal is shown in Fig. S2(f). Similarly, the DC input signal leads to a tiny output signal. Therefore, the result indicates that the share-waves vibration is not excited. Implementing DC source as an input signal to IDTs structure could lead to another characteristic such as electrostriction phenomena which could distort the lattice. However, the electrostriction phenomena can be obtained by meeting essential parameters including high DC input voltage, high electric field, tiny coupling, and low dielectric permittivity [37,38]. Therefore, the DC input voltage is not useful for our proposed devices which use the piezoelectric phenomena. In addition, it also does not meet the criteria of electrostriction phenomena.

In brief, our proposed method is focused on make the shear-wave vibration excited. Thus, the acousto-dynamic coupling in arrays AuNPs can be produced to obtain a reconfigurable LSPR spectrum. The shear-wave vibration is obtained by a matching condition between the IDT frequency with RF input signal frequency. Furthermore, an input signal with the alternate polarity between positive and negative is also required. Consequently, the DC source as an input signal is not suitable for our proposed device structure.

3. Fabrication and morphological characterization

3.1. Fabrication of arrays AuNPs on 36XY-LiTaO₃

In general, we fabricated arrays AuNPs on a 36XY-LiTaO$_3$ substrate by the following steps. The first step was to prepare a piezoelectric substrate based on 36XY-LiTaO$_3$, which was followed by Cr and Au deposition to fabricate IDTs [26]. Then, Au deposition, annealing, and quenching were performed to develop AuNPs [39]. The complete procedure is shown in Supplementary Material S2. Then, the examination of the IDT structure and electrical scattering parameter responses due to deposition of AuNPs are depicted in Supplementary Material S3 and Figs. S3(a–d). Moreover, Fig. 4(a-h) show the morphological characterization of AuNPs on a 36XY-LiTaO$_3$ substrate.

3.2. Morphological characterization

The morphology of the gold thin film before and after annealing with quenching was investigated using atomic force microscopy (AFM) (SPA-400, Seiko Instruments Inc. (SII), Japan). Before the AFM measurements, the device was ventilated using an ion removal air blower (Keyence SJ-F250., Japan). The noncontact mode of a microcantilever-type SI-DF40 K-A102002760 [Si: for DFM] (Hitachi, Japan.) was utilized.

The morphology data were visualized and analyzed using Gwydion 2.55 software [40]. Fig. 4(a) shows the detailed morphology of the AuNPs at the center of the SH-SAW device using the 2D AFM image before annealing and quenching. The height, 3D AFM image for an area of 0.04 μm^2, and particle distribution for an area of 1 μm^2 are shown in Fig. 4(b)–(d). Moreover, the morphology of the AuNPs after annealing
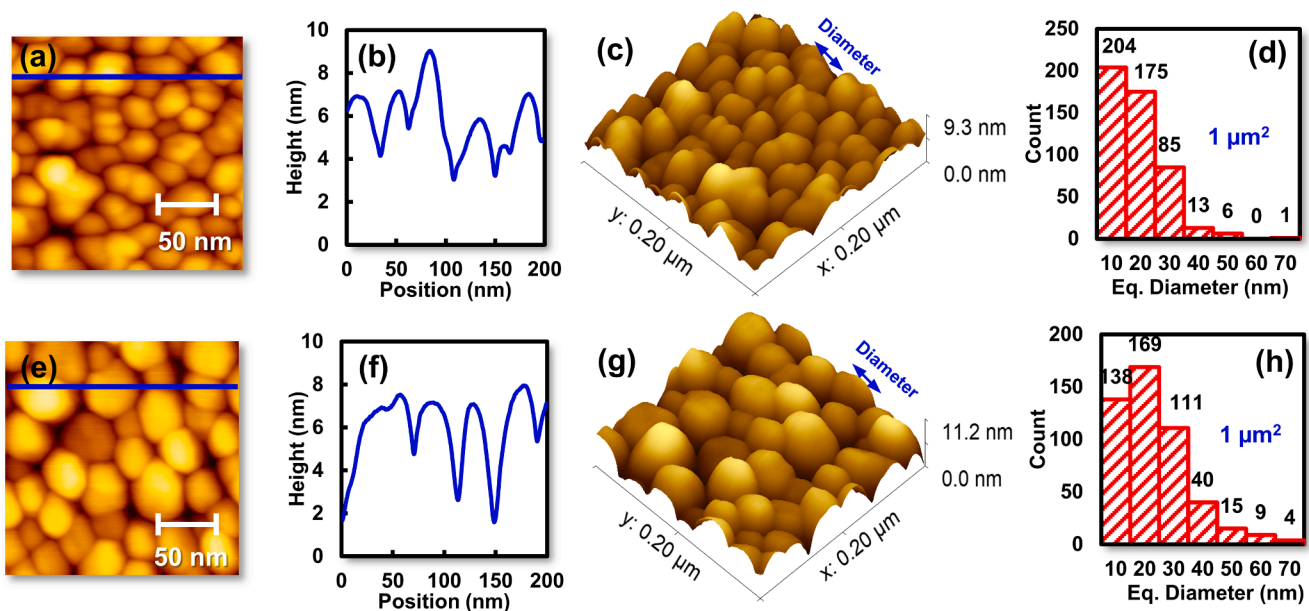

Fig. 4. The morphology of the AuNPs at the center of the SH-SAW device. The 2D AFM image, height, 3D AFM image for an area of 0.04 μm^2, and particle distribution for an area of 1 μm^2 are shown in (a)-(d) before annealing and quenching and (e)-(h) after annealing and quenching, respectively.

and quenching is depicted in Fig. 4(e)-(h). Table 1 summarizes the statistics of the surface analysis parameters for the AuNPs.

As is evident in Table 1, the data were divided into two columns of detailed information, with or without annealing and quenching. The maximum height of the surface (S_Z), average diameter equivalent (D_{EQ}), and interparticle distance (*ID*) of AuNPs from all data slightly changed. We can see that after annealing and quenching, the S_Z and D_{EQ} of AuNPs slightly increased. From the AFM measurements, the D_{EQ} value was approximately 23.16 nm, and its value could also be observed in the scanning electron microscopy (FE-SEM) morphological analysis.

3.3. Reproducing the morphological structure of the arrays AuNPs

Fig. 5(a) shows a fabricated of the proposed device including input/output IDTs and arrays AuNPs on 36XY-LiTaO$_3$ substrate. Then, the 2D morphology image of the arrays AuNPs on the propagation surface of the SH-SAW device using FE-SEM (JSM-7600F) is shown in Fig. 5(b). Moreover, in order to perform the FDTD computational analysis, we reproduced the morphological structure of AuNPs on 36XY-LiTaO$_3$ substrate base on a 2D SEM image. The structures were separated into three classifications such as; identical dimer AuNPs, nonidentical dimer AuNPs, and arrays of AuNPs structure. In details, the identical dimer AuNPs, nonidentical dimer AuNPs, and arrays AuNPs structure for OFF-condition are shown in Fig. 5(c–e), respectively. Then, the AuNPs structures with ON-condition are shown in Fig. 5(f–h). By using these approaches, we examined the plasmonic enhanced near field and LSPR spectrum.

4. FDTD computational analysis base on reproducing the morphological structure

For FDTD computational analysis, a parallel structure model was used where the direction of the light was perpendicular to the positions of the hemispherical AuNPs on the 36XY-LiTaO$_3$ substrate. Then, the AuNPs structure was reproduced from Fig. 5(c–e). In detail, the identical dimer hemispherical AuNPs, nonidentical dimer hemispherical AuNPs, and arrays hemispherical AuNPs on the 36XY-LiTaO$_3$ substrate were investigated.

4.1. Reconfigurable LSPR of identical and nonidentical dimer AuNPs

Before moving forward to simulation result, several important notes should be included. The 36XY-LiTaO$_3$ substrate has anisotropic optical characteristics and it has different characteristics compared to a glass substrate. Therefore, the refractive index value of 36XY-LiTaO$_3$ substrate has followed two principal components, including an extraordinary ray (n_e) and an ordinary ray (n_o) [41,42]. Fig. S4(a) shows the n_e, n_o, and n of the 36XY-LiTaO$_3$ substrate. Then, Fig. S4(b) illustrates the comparison of the absorption (σ_{abs}) value of AuNPs on glass and 36XY-LiTaO$_3$ subsrate. Next, Fig. S4(c) shows the simulated plasmonic enhanced near field distributions calculated. The maximum value and skin depth values (δ) normalized to the wavelength are listed in Table 2. The skin depth denotes the distance where plasmonic enhanced near

field on the AuNPs surface reaches the value of 1/e.

Fig. 6(a) and (b) show the 2D plasmonic enhanced near field of the identical dimer of AuNPs with a small interparticle distance and a large interparticle distance in an air environment, respectively. These results were obtained by FDTD simulation of identical dimer structures in Fig. 5 (c) and 5(f). The AuNPs in dimers have a hemispherical shape with a radius of r_A = 12.5 nm. We can see that a high value of 2D plasmonic enhanced near field was generated for small interparticle distance. Therefore, it has meant that a strong interaction was observed between a close couple of AuNPs that produced a plasmonic enhanced near field of 6.85 V/m. However, for the same AuNP radius, a weak 2D plasmonic enhanced near field was produced for a large AuNP dimer with a value of 3.98 V/m.

Furthermore, as mentioned above, the reconfigurable LSPR spectrum was obtained by acousto-dynamic coupling of AuNPs. Here, we use the difference interparticle distance of the dimer AuNPs (d_{A1}) to represent the acousto-dynamic coupling of AuNPs. Then, Fig. 6(c) illustrates the effect of adjusting the interparticle distance of the dimer AuNPs on the 36XY-LiTaO$_3$ substrate to the value and peak position of σ_{abs} with a constant AuNP radius of r_A = 12.5 nm. The d_{A1} was varied with 1 nm, 5 nm, 10 nm, 20 nm, and 40 nm. This result was representing the condition of Fig. 5(c) and (f). Then, Fig. 6(d) shows the σ_{abs} value and peak position for nonidentical dimer AuNPs with a radius r_A = 12.5 nm and r_B = 17.5 nm using the interparticle distance $d_{B(1)}$ as a variable. The d_{B1} was varied with same values of d_{A1}. This result was representing the condition of Fig. 5(d) and (g). We can see that the increase of interparticle distance of identical dimer and nonidentical dimer generated a blueshift effect.

4.2. Reconfigurable LSPR of arrays AuNPs using symmetric/asymmetric structure and reproducing morphological structure

Besides the dimer AuNPs composition, we also have simulated the reconfigurable LSPR based on arrays AuNPs structure. For the arrays AuNPs structure, the configuration was separated into two architectures such as symmetric/asymmetric structure and reproducing morphological structure. The symmetry structure was used to see the behavior in ordered AuNPs configuration. It was only focusing on simulation data without fabrication, as shown in Fig. 7(a–e). Moreover, the second simulation is developed base on real arrays AuNPs scheme that reproduced from morphological data in Fig. 5(e) and 5(h). The results are shown in Fig. 8(a–c).

The symmetric arrays AuNPs structure was arranged as a matrix shape using 3 lines and 6 columns with a total of 18 AuNPs. The first AuNP and the last AuNP were called A $_{(1,1)}$ and A $_{(3,6)}$, respectively, as shown in Fig. 7(a). Fig. 7(a) illustrates the near-field coupling of an array of AuNPs with symmetric relative to the T–T′ plane. We can see that symmetric arrays of AuNPs has produced a strong near-field coupling configuration. This result was examined with FDTD simulations of 2D plasmonic enhanced near field distribution, as depicted in Fig. 7(b). The symmetric arrays of AuNPs has generated a 2D plasmonic enhanced near field of 78.0 V/m.

Moreover, the existence of shear horizontal vibration has influenced the array structure. Here, the arrays of AuNPs with asymmetric structure with respect to the T–T′ plane were used to represent the effect of shear horizontal vibration. The asymmetric arrays of AuNPs configuration generate a weak near-field coupling structure, as depicted in Fig. 7(c). The FDTD simulation was utilized to verify the 2D plasmonic enhanced near field distribution of the asymmetric arrays AuNP structure, as depicted in Fig. 7(d). We can see that the asymmetric arrays of AuNPs generated a low plasmonic enhanced near field of 34.5 V/m. Furthermore, Fig. 7(e) shows the wavelength values comparison of σ_{abs} peak for symmetric/asymmetric arrays AuNPs. The blueshift effect was produced from symmetric to asymmetric arrays AuNPs.

Then, the next simulation was developed using the arrays AuNPs configuration that reproduced from a morphological structure. Fig. 8(a)
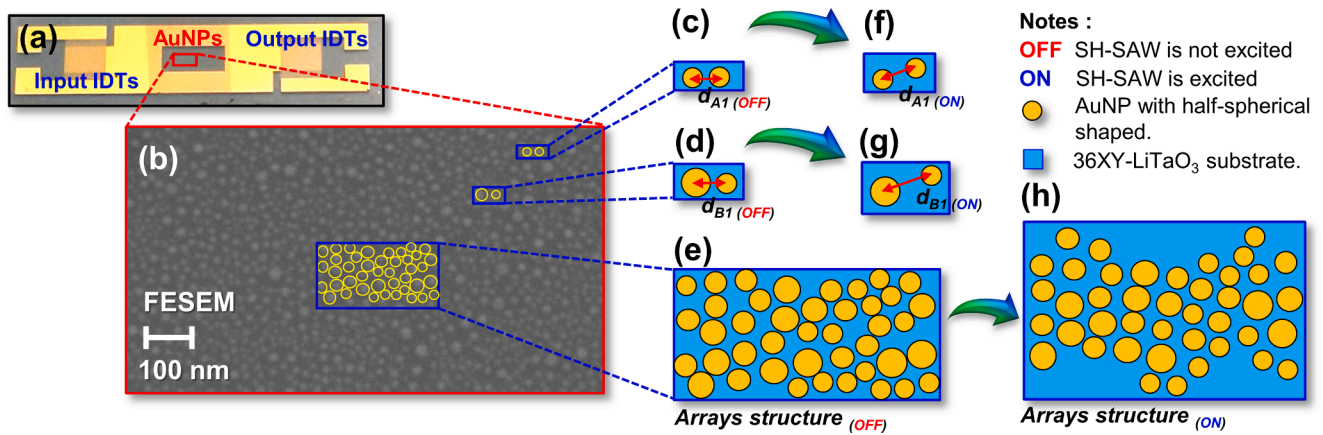
Table 1

Surface analysis parameters of AuNPs such as the amount of Au deposition, annealing, quenching, AFM capture size, number of particles (N), maximum surface height (S_Z), average equivalent diameter (D_{EQ}), and interparticle distance (ID) of AuNPs.

Method			N	S_Z (nm)	D_{EQ} (nm)	ID (nm)
Au deposition	Annealing	Quenching				
5 mg	–	–	484	9.30	18.55	45.45
5 mg	500 °C for 5 min	– 40 °C/ min	486	11.2	23.16	45.36

Fig. 5. (a) A fabricated of the proposed device including the structure of input/output IDTs and arrays AuNPs on 36XY-LiTaO$_3$ substrate, (b) the 2D the morphology image of the arrays AuNPs on the propagation surface of the SH-SAW device using FE-SEM. Reproducing the morphological AuNPs structure to (c) identical dimer AuNPs, (d) nonidentical dimer AuNPs, and (e) arrays AuNPs structure for OFF-condition. The AuNPs structure with ON-condition for (f) identical dimer AuNPs, (g) nonidentical dimer AuNPs, and (h) arrays AuNPs for ON-condition.

Table 2
Maximum E plasmonic enhanced near field and skin depth values (δ) normalized to wavelength.

Wavelength (nm)	Plasmonic enhanced near field (V/m)	δ_{AuNP} (λ)	$\delta_{36XY-LiTaO3 - air}$ (λ)
400	2.35	0.0192	0.0080
500	3.50	0.0033	0.0021
600	4.98	0.0020	0.0032
700	9.14	0.0008	0.0040
800	6.33	0.0010	0.0051
900	3.02	0.0009	0.0121

shows the 2D enhanced near field distribution from an FDTD simulation of arrays AuNPs structure for OFF-condition. It has produced a 2D plasmonic enhanced near field of 4.25 V/m. Moreover, Fig. 8(b) illustrates the 2D enhanced near field distribution from an FDTD simulation of arrays AuNPs structure for ON-condition. The ON-condition structure

was approached due to the existence of shear wave vibration. It has produced a 2D plasmonic enhanced near field of 3.93 V/m. Even the simulation structure has a higher number of particle AuNPs. However, the AuNPs particle has a random position. This condition makes the 2D plasmonic enhanced near field value significantly lower. Furthermore, Fig. 8(c) shows the wavelength values comparison of σ_{abs} peak for OFF- and ON-condition of SH-SAW, we can see that the blueshift effect was obtained. This data was also supported by higher 2D plasmonic enhanced near field for OFF-condition compared to ON-condition. Overall, the FDTD method has confirmed the reconfigurable LSPR spectrum with the result in a blueshift effect compared to the initial structures. The proposed method can be applied for multifunctional sensors with the high possibility of integration into a wireless network.

5. Conclusion

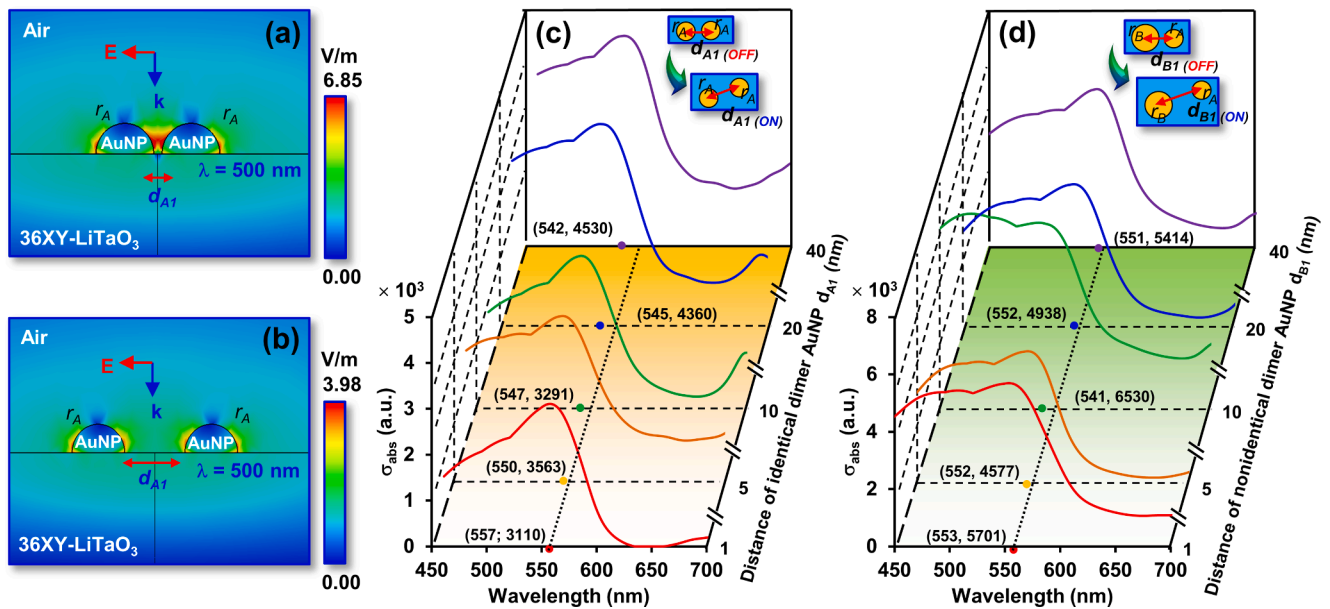We successfully developed a reconfigurable LSPR spectrum by

Fig. 6. The direction of the light was perpendicular to the positions of the hemispherical AuNPs on the 36XY-LiTaO$_3$ substrate. (a) the 2D plasmonic enhanced near field for identical dimer of hemispherical AuNPs with a small interparticle distance and (b) a large interparticle distance in an air environment. (c) The σ_{abs} values for identical dimer AuNPs with a constant radius $r_A = 12.5$ nm using the interparticle distance $d_{A(1)}$ of AuNPs as a variable. (d) The σ_{abs} values for nonidentical dimer AuNPs with a radius $r_A = 12.5$ nm and $r_B = 17.5$ nm using the interparticle distance $d_{B(1)}$ as a variable.
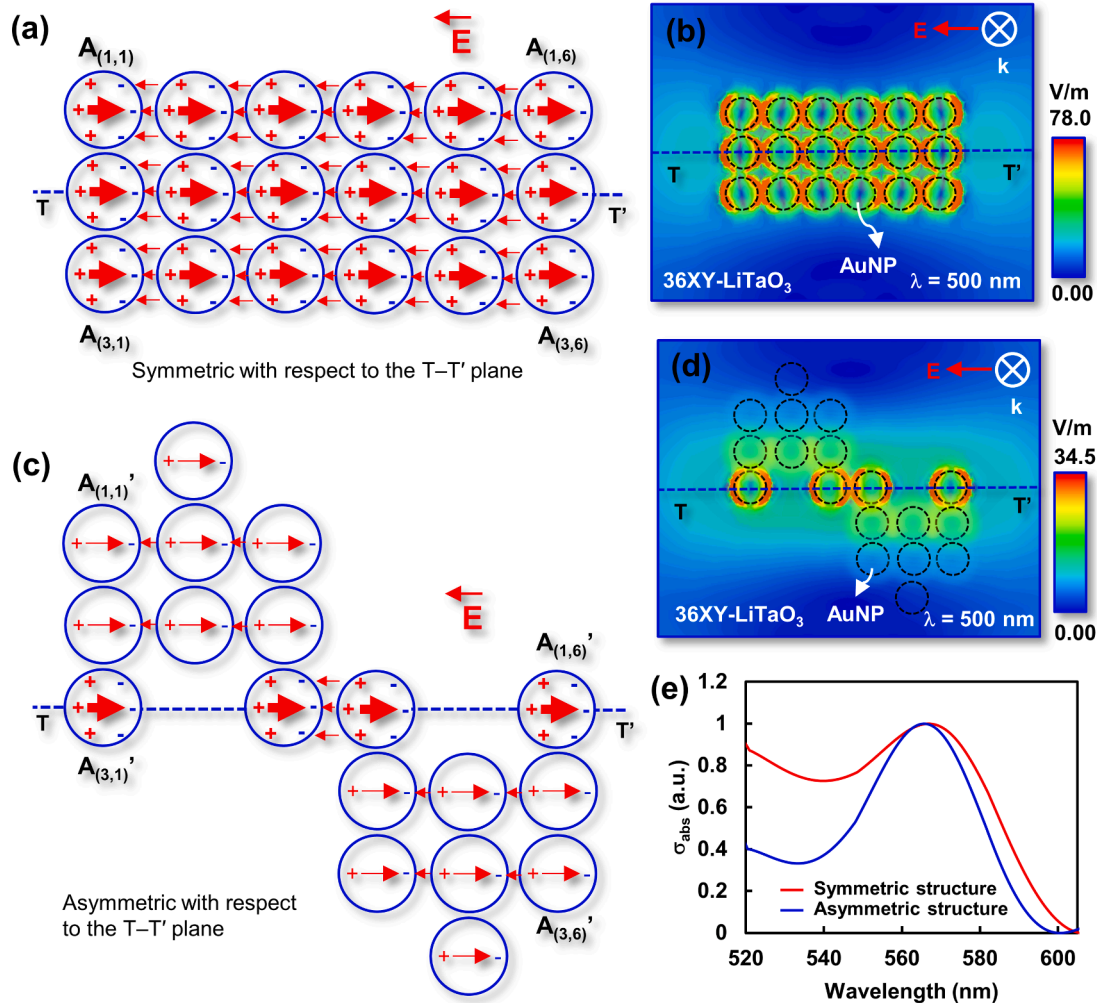
Fig. 7. The symmetric arrays AuNPs with the first AuNP and the last AuNP are called A$_{(1,1)}$ and A$_{(3,6)}$, respectively. (a) An array of AuNPs with symmetric relative to the T–T′ plane and near-field coupling structure, (b) the 2D enhanced near field distribution from an FDTD simulation of an AuNP array with symmetric structure with respect to the T–T′ plane, (c) an array of AuNPs with asymmetric structure relative to the T–T′ plane, and near-field coupling structure, (d) the 2D enhanced near field distribution from an FDTD simulation of an AuNP array with asymmetric structure with respect to the T–T′ plane, (e) the wavelength values comparison of σ_{abs} peak for symmetric/asymmetric arrays AuNPs.
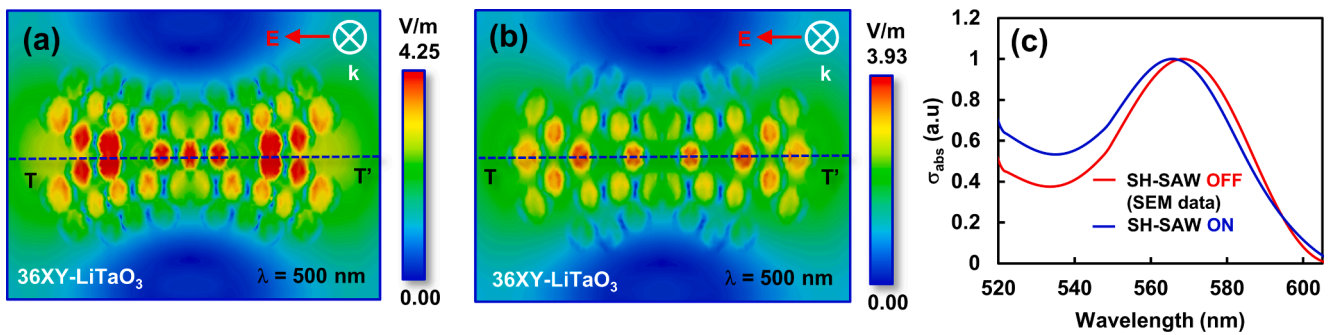

Fig. 8. (a) The 2D enhanced near field distribution from an FDTD simulation of arrays AuNPs structure for OFF-condition, (b) the 2D enhanced near field distribution from an FDTD simulation of arrays AuNPs structure for ON-condition, (c) the wavelength values comparison of σ_{abs} peak for OFF- and ON-condition of SH-SAW.

acousto-dynamic coupling in arrays of AuNPs induced by shear-horizontal vibrations. The vibrations were produced by piezoelectric phenomena. The experimental results demonstrated that the ON-condition produced a blueshift effect on the peak position with an adjustment quality factor compared to the OFF condition. Moreover, we also have reproduced the morphological structure of array AuNPs from

SEM images. The structures were separated as identical dimer AuNPs, nonidentical dimer AuNPs, and arrays AuNPs on the 36XY-LiTaO$_3$ substrate. The FDTD computational analysis has confirmed that the reconfigurable LSPR spectrum was produced with a blueshift effect compare to the initial structures. The proposed method has several advantages, such as being tenable and having a high possibility for

multifunctional sensor applications.

6. Authorship contributions

T.F. conducted the concept, simulation, experiments, and formal analysis. The obtained results were discussed and evaluated by T.H, G. W., E.T.R. and J.K. T.F. wrote the original manuscript and drew all the illustration of original manuscript. G.W., and E.T.R, reviewed and editing. J.K. funding, reviewed, and editing. All authors have been read and agreed to the publised version of the manuscript.

Declaration of Competing Interest

The authors declare that they have no known competing financial interests or personal relationships that could have appeared to influence the work reported in this paper.

Data Availability Statement

The data that support the findings of this study are available from the corresponding author upon reasonable request.

Appendix A. Supplementary material

Supplementary data to this article can be found online at https://doi.org/10.1016/j.apsusc.2021.151331.

References

[1] A.V. Kabashin, P. Evans, S. Pastkovsky, W. Hendren, G.A. Wurtz, R. Atkinson, R. Pollard, V.A. Podolskiy, A.V. Zayats, Plasmonic nanorod metamaterials for biosensing, Nat. Mater. 8 (2009) 867–871, https://doi.org/10.1038/nmat2546.

[2] D.C. Marinica, M. Zapata, P. Nordlander, A.K. Kazansky, P.M. Echenique, J. Aizpurua, A.G. Borisov, Applied Optics: Active quantum plasmonics, Sci. Adv. 1 (2015) 1–7, https://doi.org/10.1126/sciadv.1501095.

[3] R. Hong, X. Wang, J. Ji, C. Tao, R. Zhang, D. Zhang, ITO induced tunability of surface plasmon resonance of silver thin film, Appl. Surf. Sci. 356 (2015) 701–706, https://doi.org/10.1016/j.apsusc.2015.08.135.

[4] Y. Li, Y. Yan, Y. Li, H. Zhang, D. Li, D. Yang, Size-controlled synthesis of Pd nanosheets for tunable plasmonic properties, CrystEngComm. 17 (2015) 1833–1838, https://doi.org/10.1039/c4ce02062f.

[5] S. Ghosh, M. Saha, V.D. Ashok, B. Dalal, S.K. De, Tunable surface plasmon resonance in Sn-Doped Zn-Cd-O alloyed nanocrystals, J. Phys. Chem. C. 119 (2015) 1180–1187, https://doi.org/10.1021/jp5107873.

[6] J. Chen, Y. Ren, T. Hu, T. Xu, Q. Xu, Fabrication and application of substoichiometric tungsten oxide with tunable localized surface plasmon resonances, Appl. Surf. Sci. 465 (2019) 517–525, https://doi.org/10.1016/j.apsusc.2018.09.140.

[7] M.E. Koleva, N.N. Nedyalkov, D. Karashanova, G.B. Atanasova, A.L. Stepanov, Modification of plasmon resonance properties of noble metal nanoparticles inside the glass matrices, Appl. Surf. Sci. 475 (2019) 974–981, https://doi.org/10.1016/j.apsusc.2019.01.051.

[8] M. Focsan, A. Campu, A.M. Craciun, M. Potara, C. Leordean, D. Maniu, S. Astilean, A simple and efficient design to improve the detection of biotin-streptavidin interaction with plasmonic nanobiosensors, Biosens. Bioelectron. 86 (2016) 728–735, https://doi.org/10.1016/j.bios.2016.07.054.

[9] A. Farnood, M. Ranjbar, H. Salamati, Localized surface plasmon resonance (LSPR) detection of hydrogen gas by Pd2+/Au core/shell like colloidal nanoparticles, Int. J. Hydrogen Energy. 45 (2020) 1158–1169, https://doi.org/10.1016/j.ijhydene.2019.10.168.

[10] Y. You, S. Lim, S. Gunasekaran, Streptavidin-Coated Au Nanoparticles Coupled with Biotinylated Antibody-Based Bifunctional Linkers as Plasmon-Enhanced Immunobiosensors, ACS Appl. Nano Mater. 3 (2020) 1900–1909, https://doi.org/10.1021/acsanm.9b02461.

[11] K.M. Mayer, J.H. Hafner, Localized surface plasmon resonance sensors, Chem. Rev. 111 (2011) 3828–3857, https://doi.org/10.1021/cr100313v.

[12] I. Saleem, W. Widger, W.K. Chu, A new technique to detect antibody-antigen reaction (biological interactions) on a localized surface plasmon resonance (LSPR) based nano ripple gold chip, Appl. Surf. Sci. 411 (2017) 205–209, https://doi.org/10.1016/j.apsusc.2017.03.115.

[13] L. Guo, D.H. Kim, LSPR biomolecular assay with high sensitivity induced by aptamer-antigen-antibody sandwich complex, Biosens. Bioelectron. 31 (2012) 567–570, https://doi.org/10.1016/j.bios.2011.10.047.

[14] R.V. Nair, P.J. Yi, P. Padmanabhan, B. Gulyás, V.M. Murukeshan, Au nano-urchins enabled localized surface plasmon resonance sensing of beta amyloid fibrillation, Nanoscale Adv. 2 (2020) 2693–2698, https://doi.org/10.1039/d0na00164c.

[15] M. Sui, S. Kunwar, P. Pandey, J. Lee, Strongly confined localized surface plasmon resonance (LSPR) bands of Pt, AgPt, AgAuPt nanoparticles, Sci. Rep. 9 (2019) 1–14, https://doi.org/10.1038/s41598-019-53292-1.

[16] C.Y. Chang, H.T. Lin, M.S. Lai, T.Y. Shieh, C.C. Peng, M.H. Shih, Y.C. Tung, Flexible Localized Surface Plasmon Resonance Sensor with Metal–Insulator–Metal Nanodisks on PDMS Substrate, Sci. Rep. 8 (2018) 1–8, https://doi.org/10.1038/s41598-018-30180-8.

[17] N. Jiang, X. Zhuo, J. Wang, Active Plasmonics: Principles, Structures, and Applications, Chem. Rev. 118 (2018) 3054–3099, https://doi.org/10.1021/acs.chemrev.7b00252.

[18] S. Khatua, W.S. Chang, P. Swanglap, J. Olson, S. Link, Active modulation of nanorod plasmons, Nano Lett. 11 (2011) 3797–3802, https://doi.org/10.1021/nl201876r.

[19] Y. Zhao, T. Walker, Y.B. Zheng, S.C.S. Lin, A.A. Nawaz, B. Kiraly, J. Scott, T. J. Huang, Mechanically tuning the localized surface plasmon resonances of gold nanostructure arrays, J. Nanotechnol. Eng. Med. 3 (2012) 1–5, https://doi.org/10.1115/1.4006616.

[20] M.A. Mahmoud, Polarized Optomechanical Response of Silver Nanodisc Monolayers on an Elastic Substrate Induced by Stretching, J. Phys. Chem. C. 119 (2015) 19359–19366, https://doi.org/10.1021/acs.jpcc.5b05359.

[21] A. Mizuno, A. Ono, Static and dynamic tuning of surface plasmon resonance by controlling interparticle distance in arrays of Au nanoparticles, Appl. Surf. Sci. 480 (2019) 846–850, https://doi.org/10.1016/j.apsusc.2019.03.058.

[22] H.I. Muri, D.R. Hjelme, LSPR coupling and distribution of interparticle distances between nanoparticles in hydrogel on optical fiber end face, Sensors (Switzerland). 17 (2017) 1–19, https://doi.org/10.3390/s17122723.

[23] N. Gisbert Quilis, M. van Dongen, P. Venugopalan, D. Kotlarek, C. Petri, A. Moreno Cencerrado, S. Stanescu, J.L. Toca Herrera, U. Jonas, M. Möller, A. Mourran, J. Dostalek, Actively Tunable Collective Localized Surface Plasmons by Responsive Hydrogel Membrane, Adv. Opt. Mater. 7 (2019), https://doi.org/10.1002/adom.201900342.

[24] K.C. Chu, C.Y. Chao, Y.F. Chen, Y.C. Wu, C.C. Chen, Electrically controlled surface plasmon resonance frequency of gold nanorods, Appl. Phys. Lett. 89 (2006) 2012–2015, https://doi.org/10.1063/1.2335812.

[25] P.A. Kossyrev, A. Yin, S.G. Cloutier, D.A. Cardimona, D. Huang, P.M. Alsing, J. M. Xu, Electric field tuning of plasmonic response of nanodot array in liquid crystal matrix, Nano Lett. 5 (2005) 1978–1981, https://doi.org/10.1021/nl0513535.

[26] T. Firmansyah, G. Wibisono, E.T. Rahardjo, J. Kondoh, Multifunctional and sensitivity enhancement of hybrid acoustoplasmonic sensors fabricated on 36XY-LiTaO$_3$ with gold nanoparticles for the detection of permittivity, conductivity, and the refractive index, ACS Appl. Mater. Interf. 13 (2021) 13822–13837, https://doi.org/10.1021/acsami.1c00110.

[27] G. Greco, M. Agostini, R. Shilton, M. Travagliati, G. Signore, M. Cecchini, Surface acoustic wave (SAW)-enhanced chemical functionalization of gold films, Sensors (Switzerland) 17 (2017) 1–11, https://doi.org/10.3390/s17112452.

[28] C.S. Chiu, H.Y. Chen, C.F. Hsiao, M.H. Lin, S. Gwo, Ultrasensitive surface acoustic wave detection of collective plasmonic heating by close-packed colloidal gold nanoparticles arrays, J. Phys. Chem. C. 117 (2013) 2442–2448, https://doi.org/10.1021/jp3030864.

[29] J.A. De Feijter, J. Benjamins, The propagation of surface shear waves. II. Experiments, J. Colloid Interf. Sci. 70 (1979) 375–382, https://doi.org/10.1016/0021-9797(79)90041-9.

[30] J. Chen, S. Shi, R. Su, W. Qi, R. Huang, M. Wang, L. Wang, Z. He, Optimization and application of reflective LSPR optical fiber biosensors based on silver nanoparticles, Sensors (Switzerland) 15 (2015) 12205–12217, https://doi.org/10.3390/s150612205.

[31] S. Kunwar, P. Pandey, Enhanced localized surface plasmon resonance of fully alloyed AgAuPdPt, AgAuPt, AuPt, AgPt, and Pt nanocrystals: systematical investigation on the morphological and LSPR properties of Mono-, Bi-, Tri-, and quad-metallic nanoparticles, ACS Omega 4 (2019) 17340–17351, https://doi.org/10.1021/acsomega.9b02066.

[32] V.A. Fedotov, V.I. Emel'yanov, K.F. MacDonald, N.I. Zheludev, Optical properties of closely packed nanoparticle films: Spheroids and nanoshells, J. Opt. A Pure Appl. Opt. 6 (2004) 155–160, https://doi.org/10.1088/1464-4258/6/2/001.

[33] S.A. Kovalenko, Optical properties of thin gold films, Semicond. Phys. Quant. Electron. 3 (2000) 383–388, https://doi.org/10.15407/spqeo3.03.383.

[34] B. Chen, H. Guo, C. Liu, L. Shang, X. Ye, L. Chen, C. Feng, K. Hayashi, Molecularly imprinted sol-gel/Au@Ag core-shell nano-urchin localized surface plasmon resonance sensor designed in reflection mode for detection of organic acid vapors, Biosens. Bioelectron. 169 (2020), 112639, https://doi.org/10.1016/j.bios.2020.112639.

[35] A. Albareda, R. Pérez, Non-linear behaviour of piezoelectric ceramics, Springer Ser. Mater. Sci. 140 (2011) 681–726, https://doi.org/10.1007/978-90-481-2875-4_15.

[36] D.A Hall, Review nonlinearity in piezoelectric ceramics, J. Mater. Sci. 36 (2001) 4575–4601, https://doi.org/10.1023/A:1017959111402.

[37] S. Santucci, V. Esposito, Electrostrictive Ceramics and Their Applications, Encycl. Mater. Tech. Ceram. Glas. (2021) 369–374, https://doi.org/10.1016/b978-0-12-803581-8.12071-5.

[38] R.E. Newnham, V. Sundar, R. Yimnirun, J. Su, Q.M. Zhang, Electrostriction: Nonlinear electromechanical coupling in solid dielectrics, J. Phys. Chem. B. 101 (1997) 10141–10150, https://doi.org/10.1021/jp971522c.

[39] T. Handoyo, J. Kondoh, Enhancement of ultrathin localized surface plasmon resonance sensitivity using sequential temperature treatment for liquids sensing, Sens. Actuat. A Phys. 307 (2020), 112006, https://doi.org/10.1016/j.sna.2020.112006.

[40] Http://gwyddion.net/, http://gwyddion.net/, Version 2.56. (2020). http://gwyddion.net/ (accessed April 17, 2020).

[41] Deng-Ke Yang, Shin-Tson Wu. Fundamentals of Liquid Crystal Devices, 2nd ed., John Wiley & Sons, 2015.

[42] P. García Parejo, A. Álvarez-Herrero, Liquid crystals for space instrumentation: optical properties of liquid crystal mixtures for polarimeters, Opt. Mater. Exp. 9 (2019) 2681, https://doi.org/10.1364/ome.9.002681.